



“Gamma Irradiation Synthesis of Carboxymethyl Chitosan-Nanoclay Hydrogel for the Removal of Cr(VI) and Pb(II) from Aqueous Media”

Manar El-Sayed Abdel-Raouf¹ · Rasha S. Kamal¹ · Dalia E. Hegazy² · Asmaa Sayed²

Received: 20 December 2022 / Accepted: 11 January 2023 / Published online: 1 March 2023
© The Author(s) 2023

Abstract

Hydrogel composites comprised of N,O carboxymethyl chitosan crosslinked with different weight ratios of acrylic acid and fabricated with nanoclay particle were prepared via gamma irradiation at 25 kGy irradiation dose. The prepared composites were coded as CsAA₁Cl, CsAA₂Cl and CsAA₃Cl based on the weight ratio of acrylic acid to the chitosan derivative. The claimed hydrogels were characterized by FTIR, TGA and XRD. The TGA data implied that the incorporation of clay nanoparticles enhanced the thermal stability of the composites; the decomposition temperature increased up to 500 °C for CsAA₃Cl. Three AFM outcomes were used to compare the surface features of the samples; topography, height and surface roughness. The topography data reveals that the nanoclay particles incorporated in CsAA₃Cl are intercalated and exfoliated. Then, the optimized sorbent (CsAA₃Cl) was investigated as green sorbents for chromium (VI) and lead (II). The data revealed that CsAA₃Cl displayed maximum removal performance towards both lead and chromium with removal efficiencies 125 mg/g and 205 mg/g respectively at the optimum application conditions within 90 min only. Also, it was found that the optimum pH value was 9 for chromium and 8 for lead. The data proved that the adsorption of both cations followed pseudo-first order kinetic model. The prepared composites showed acceptable metal uptake capacity at three successive cycles.

Keywords N, O carboxymethyl chitosan · Acrylic acid · Clay · Chromium (VI) · Lead (II) · AFM

1 Introduction

The utilization of natural polymers such as chitosan, starch and cellulose has attracted great attention to achieve sustainability and to fulfill the SDGs that have been previously announced by the United Nation [1–3]. Green polymers are very advantageous due to their biodegradability, biocompatibility and high functionality that enables formation of enormous number of modified products to fit different applications [4–9]. Wastewater remediation is one of the most important fields that the natural polymer can be applied in. Indeed, the term (wastewater) is a very wide term because it includes different sub-categories such as industrial wastewater, household wastewater, agricultural wastewater...etc

[10–13]. However, all types of wastewater include numerous pollutants that threaten human health directly and indirectly when escaped to the food-web. Heavy metals are among the most potent toxic materials found in wastewater. The term (heavy metals) denotes naturally occurring elements with high atomic weight and possess density heavier than that of water at least five folds [14–16]. They are widely distributed in the environment due to their universal utilization in several industries [17, 18]. The top five toxic heavy metal are; *arsenic, cadmium, chromium, lead, and mercury*. They are recognized to persuade multiple organ damage, even at lower levels of exposure. They are also classified as human carcinogens (known or probable) according to the US. Environmental Protection Agency, and the International Agency for Research on Cancer [19, 20]. Therefore, elimination of these metals from aqueous solutions was the top topic of many research works [13, 21–24]. There are several methods applied for wastewater treatment; such as coprecipitation [25], cation exchange [26], Ultrafiltration [27], reverse osmosis [28], nanofiltration [29], adsorption–reduction [30] and adsorption [31]. From economic and environmental points of view, application of adsorbent materials

✉ Rasha S. Kamal
dr.rasha_samir@yahoo.com

¹ Department of Petroleum Applications, Egyptian Petroleum Research Institute, Nasr City, Cairo, Egypt

² Polymer chemistry department, National Center for Radiation Research and Technology, Egyptian Atomic Energy Authority, Cairo, Egypt

is advantageous over other methods due to ease of application, feasibility, broadness of adsorbents, recyclability, and lack of production of biproducts [32–36]. Sorbents based on natural materials have been extensively used in removal of heavy metals [29, 37–45]. Chitin is the third abundant natural polymer after cellulose and starch [46]. It can be adapted into chitosan by simple deacetylation protocol. Chitosan is a highly functional amino-carbohydrate polymer [47]. It has been modified into different products to eliminate various types of pollutants from wastewater [48, 49]. It is well established that increasing the functionality of chitosan by chemical modification improves its ability to remove different categories of pollutants [50]. Moreover, formation of chitosan-based crosslinked porous structure enhances the sorption efficiency of modified chitosan [51]. On the other hand, incorporation of inorganic core such as metal oxides, carbon nanotubes and clay into the polymer matrix modifies the mechanical and thermal properties of the network to be used for consequent cycles [52]. Generally, crosslinking process may take place either thermally or under the effect of irradiations such as gamma and electron beam irradiations [53]. It is believed that gamma irradiation is one of the most desired crosslinking protocols due to its high effectiveness and greenness [54].

In the present work, three hydrogels based on N, O carboxymethyl chitosan/crosslinked acrylic acid enforced with Kaolinite (the term “clay” will be applied throughout this work) were prepared via gamma irradiation at 25 kGy, and evaluated as green sorbents for two potent toxic metals; chromium and lead at different experimental conditions. The claimed hydrogels were characterized with different techniques. The pseudo first and second order kinetic models were applied to describe the nature of the adsorption process. Moreover, Langmuir and Freundlich adsorption models were verified in order to understand the mechanism of removal process. Thus, the novelty of this work relies on utilization of green components by environmentally friendly protocol to be used as effective sorbents for two model poisonous elements from their aqueous solutions as an attempt to create potent sorbents for industrial wastewater treatment. Moreover, the metal uptake process was proved by the AFM by comparing the surface features of the metal-free and metal-loaded hydrogels.

2 Experimental

2.1 Materials

Chitosan (deacetylation degree of 88% and a m.wt. of $1.0\text{--}3.0 \times 10^5$ g/mol) obtained from Merck, α -ketoglutaric acid (analytical grade white powder) obtained from Sigma-Aldrich, Glacial Acetic acid (Ultrapure (99.9%))

colorless liquid with pungent odor) purchased from Al-Nasr company for chemical industries, Egypt. Acrylic acid was acquired from Sigma-Aldrich as analytical reagent colorless liquid. Potassium dichromate (99% pure reddish orange crystals), lead nitrate (analytical grade white powder) and Sodium borohydride (ultrapure powder 99.9%) were obtained from Merck. The clay (Kaolinite, $\text{Al}_2\text{Si}_2\text{O}_5(\text{OH})_4$) with average particle size range 50–75 nm was supplied from El-Nasr company for mining and used without further processing.

2.2 Preparation of N,O Carboxymethyl Chitosan

A facile method was applied. Shortly, a solution of 5% chitosan in 1% acetic acid was prepared. Then, 8 g α -ketoglutaric acid was gradually added with continuous stirring at pH 5.0. The reaction was continued for 4 h at room temperature and pH was adjusted to neutral. The reaction was continued for 12 h at 50 °C. Lastly, the product was separated, filtered and washed with ethanol, then the dried solid N,O- carboxymethyl chitosan (N,O-CMCs) was obtained after vacuum drying. The degree substitution of N,O-CMCs was calculated by potentiometric titration method ($39.2 \pm 0.7\%$).

2.3 Preparation of the Chitosan-Based Hydrogel Enforced with Nanoclay

Three formulations have been prepared by varying the weight ratio between carboxymethyl chitosan (CMCs) and acrylic acid (AA). Briefly, 1 gm of carboxymethyl chitosan is completely dissolved in 100 ml acidified water. Then, the desired amount of acrylic acid is added (1–3 gm) with continuous stirring for 30 min at 600–700 rpm. A mass of 0.25 g nanoclay was added with careful stirring then sonication for 60 min to assure complete miscibility. Next, the solution is transferred into glass tubes and subjected to ^{60}Co -gamma rays at 25 kGy irradiation dose for synthesis of the crosslinked chitosan. The hydrogels were removed from the tubes and cut into regular discs. The codes and composition of the prepared architects are illustrated in Table 1.

Table 1 Codes and composition of the green hydrogel composites

Code	CMCs (g)	AA (g)	Clay (g)	Irradiation dose (kGy)
CsAA ₁ Cl	1	1	0.25	25
CsAA ₂ Cl	1	2	0.25	25
CsAA ₃ Cl	1	3	0.25	25

2.4 Characterization

The surface morphology and topography were imaged by using an AFM, model Flexaxiom Nanosurf, C3000. The images were taken by contact mode using a NCLR cantilever at frequency 9 kHz. The surface area, average pore volume and average pore size of the prepared adsorbents were measured by BILSORB-Minix at 350 °C using the Brunauer–Emmett–Teller (BET) equations and Dubinin–Astakhov method.

The surface features of chitosan composites were photographed using the high-resolution Field emission-scanning electron microscope (JSM-7610 F). The photographing took place at an accelerated voltage of 15 kV.

The FTIR spectra of the modified and crosslinked chitosan were recorded by FTIR spectrometer Nicolet 6700 (Thermo Scientific). The samples were mixed separately with KBr powder and then crushed under a hydraulic pressure of 400 kg cm⁻² then shaped in the form of pellets. The spectra were verified at the range 4000–400 cm⁻¹, at room temperature.

The crystalline features of the prepared composites were checked via X-ray diffractometer (Rigaku Ultima-IV). The powder of each sample was placed onto the sample holder and scanned in the reflection mode at a 2θ angle over a range from 5° to 90° at a speed of 10°/min. The thermal stability was investigated by ELTRA's TGA Thermostep ML at the temperature range 0–600 °C with rate of heating 10 °C/min.

2.5 Adsorption Investigation

2.5.1 Preparation of Solutions

Stock solution of Cr(VI), and Pb(II) (0.01 mol/L)-were prepared by dissolving K₂Cr₂O₇, PbNO₃ separately in distilled water. For conducting the batch experiments, stock solution of the metal ions was diluted to the desired concentration. The pH value of the aqueous solutions was adjusted by adding small amounts of HCl or NaOH solutions.

2.5.2 Removal Performance Test

Metal ion adsorption was carried out by adding 0.05 g of chitosan modified product into 50 mL of (25 ppm, 50 ppm, 75 ppm, 100 ppm) of metal ion solution. The percentage of removal is monitored by withdrawing one ml of the solution at a predetermined time and the remaining concentration of the metal after adsorption was measured using atomic adsorption spectrometer (AAS). The percentage removal (R%), and the adsorption capacity (q_e) of the metal ion can be calculated from the following Equations.:

$$\%R = \frac{C_0 - C_e}{C_e} \times 100 \quad (1)$$

$$q_e = C_0 - C_e \times \frac{V}{m} \quad (2)$$

where q_e is the amount of metal adsorbed onto the sorbent at the equilibrium, C₀ and C_e (mg/L) are the original concentration of metal cation and at equilibrium, respectively and V (L) is the volume of metal ion solution, m (g) is the weight of adsorbent. The batch adsorption isotherms were studied as previous at pH 7, at the metal ions concentration 25–100 mg/L at 25 °C. The removal efficiency was investigated at pH range 1–9 for Cr (VI) and from 4 to 11 for Pb (II) and at temperature range 25–45 °C.

2.6 Reusability Experiments

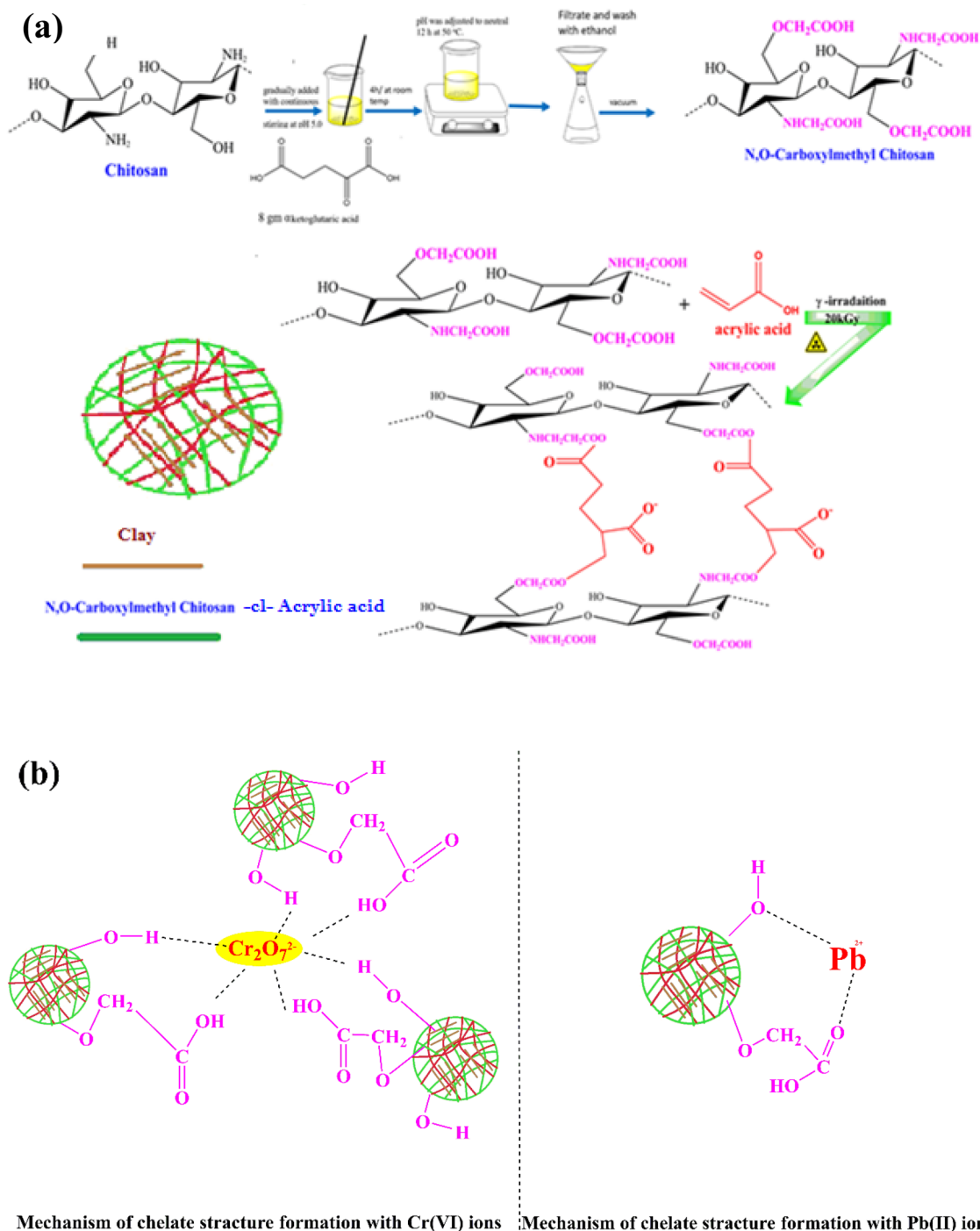
The metal loaded sorbent was immersed in 20 mL of 1 N HCl for 60 at 250 rpm stirring speed under ambient temperature to ensure complete desorption. The sorbent was recovered from the solution by filtration and was carefully washed with double distilled water and reused in three successive cycles. The metal ion in the filtrate was measured by AAS. The reusability efficiency (%) was computed from Eq. (3).

$$\text{The reusability efficiency(\%)} = \frac{\text{Metal uptake in round (n + 1)}}{\text{Metal uptake in round (n)}} \times 100 \quad (3)$$

3 Results and Discussion

3.1 Preparation of the Hydrogel Nanocomposites

Chitosan modified products are widely known in wastewater remediation [55–58]. However, functionalization of chitosan via carboxymethylation affords more stronger reactive groups (such as carbonyl group) which can form stable chelate structures with various metal cations [59]. Moreover, formation of porous structure enhances the metal uptake capacity of the sorbent material due to multi-void architects [60]. The incorporation of inorganic support into the hydrogel matrix protects the hydrogel from being teared at subsequent swelling-deswelling cycles [61]. Nanoclay particles are classified among the efficient sorbents for different contaminants [62]. Therefore, the present work combines the benefits of many components in one crosslinked structure enforced with clay nanoparticles. It is worthy to mention that gamma irradiation was used at 25 kGy to initiate and induce crosslinking. This dose was proved effective enough to form feasible crosslinked structure with suitable degree of crosslinking and surface features as per our previous work [8]. Yet, the ratio of acrylic acid to chitosan was



Scheme 1 **a** Proposed mechanism of hydrogel formation, **b** metal uptake process

varied in order to investigate the effect of this change on the morphology and surface features of the hydrogel matrix in order to nominate the optimized composite according to these features.

The proposed scheme for synthesis of the green nanocomposites is illustrated in Scheme 1a and the proposed mechanism of metal uptake process is displayed in scheme 1b.

3.2 Optimization of the Hydrogel Composite via the AFM

3.2.1 AFM Characterization of Surface Features due to Composite Formation

The topography and surface morphology of dry clay, N, O CMCs and CsAA₁Cl were investigated by the AFM to

illustrate the difference in surface features as a result of composite formation, (Fig. 1a–c). The AFM images were further analyzed by Gwyddion software to give the best possible view of phase changes, Fig. 1d–f. Based on topography and surface features, it can be seen that the nanoclay particles appear as sharp particulates, the surface of N, O CMCs appear as relatively rough striated morphology. While the AFM image of CsAA₁Cl reveals crosslinked structure with humps and pores which confirm the formation of three-dimensional network with included clay nanoparticles. The images which are analyzed with Gwyddion display the number and morphology of the phases comprising the investigated samples. The clay nanoparticles appear as sharp projected crystal, and the surface of N, O CMCs shows smooth uniform look and the surface of CsAA₁Cl depicts three different phases. These observations strongly confirm our previous findings [63, 64]. Moreover, two major AFM outcomes are considered; the height and the roughness measurements, Table 2. These parameters were specifically selected because they confirm the chemical modification.

It can be observed that the height measurements of clay nanoparticles and N,O CMCs are very close which reveal the similar crystalline nature, this observation confirms that the carboxymethylation of chitosan slightly decreases the crystallinity of chitosan. On the other hand, the height of the crosslinked composite is about four folds than the functionalized product which confirms the formation of porous structure. In contrary to the height measurements, the area roughness of the samples are in the order: Clay nanoparticles > the crosslinked CsAA₁₋₃Cl > N,O CMCs.

3.2.2 Topography Changes in Accordance to N, O CMCs/AA Ratio

AFM outcomes (roughness and height measurements) were used in order to select the optimum hydrogel composite. In this regard, the AFM images of CsAA₂Cl, and CsAA₃Cl are given in Fig. 1g and h and the AFM data of these composites are tabulated in Table 2. Upon comparing all the AFM outcomes, it can be deduced that the optimum hydrogel composite according to the height and roughness measurements is CsAA₃Cl. In our previous works [6, 7] we found that the

height reflects the pore volume and the optimum hydrogel must possess suitable pore volume and proper pore distribution with acceptable surface roughness to achieve the maximum metal uptake capacity. It is established that moderate height reflects suitable pore size possible for capturing the adsorbate molecule tightly which can escape easily from wide pores. Also, the AFM image of CsAA₃Cl (Fig. 1h) displays the clay nanoparticles as white patches over the surface that reveals that the nanoclays are intercalated and exfoliated.

3.3 Total Surface Area and Average Pore Volume

The internal structures of the prepared sorbents were investigated using BET measurements via the N₂ adsorption–desorption isotherm methodology. The BET surface area and Dubinin–Astakhov average pore volume and average pore diameter are tabulated in Table 3. It can be noticed that the investigated parameters (total surface area, average pore volume and average pore diameter) increased by increasing the content of acrylic acid which infers higher degree of crosslinking. The data showed that the measurements obtained for CsAA₃Cl are the highest which reveals that this sorbent possess a more developed pore structure and more abundant adsorption sites, thus dropping the mass transfer resistance in the adsorption process and levelling up the adsorption. This finding may assist the data of the metal uptake provided in the next sections. It is stated that the porosity can be controlled by adjusting the degree of crosslinking [7].

3.4 Surface Investigation via Field Emission-Scanning Electron Microscope

The morphology of CsAA₃ and CsAA₃Cl was investigated via the FE-SEM, Fig. 2a and b respectively. It can be seen that the clay particles appear as minute masses distributed within the matrix and also as tiny hairy projections emerged over the surface which reveal that the clay is scattered inside and above the gel matrix. This finding is consistent with the AFM observation regarding the distribution of the clay nanoparticles.

3.5 IR Characterization of the Hydrogel Nanocomposites

The IR spectra of Clay, N, O carboxymethyl chitosan and CsAA₃Cl are provided in Fig. 3. Upon investigating the IR spectrum of clay, some significant peaks that lie at the range 500–550 cm⁻¹ are assigned for Si–O–Al and Si–O–Si [65, 66]. Other important peaks appear in the range 3200–3300 cm⁻¹. These peaks were overlapped with the peaks assigned for O–H, N–H and acidic O–H which

Table 2 Some AFM outcomes

Sample	Height (nm)	Ra (nm)
Clay nanoparticles	4.56	28.11
N, O CMCs	4.72	13.78
CsAA ₁ Cl	17.8	19.16
CsAA ₂ Cl	19.1	18.33
CsAA ₃ Cl	25.8	16.21

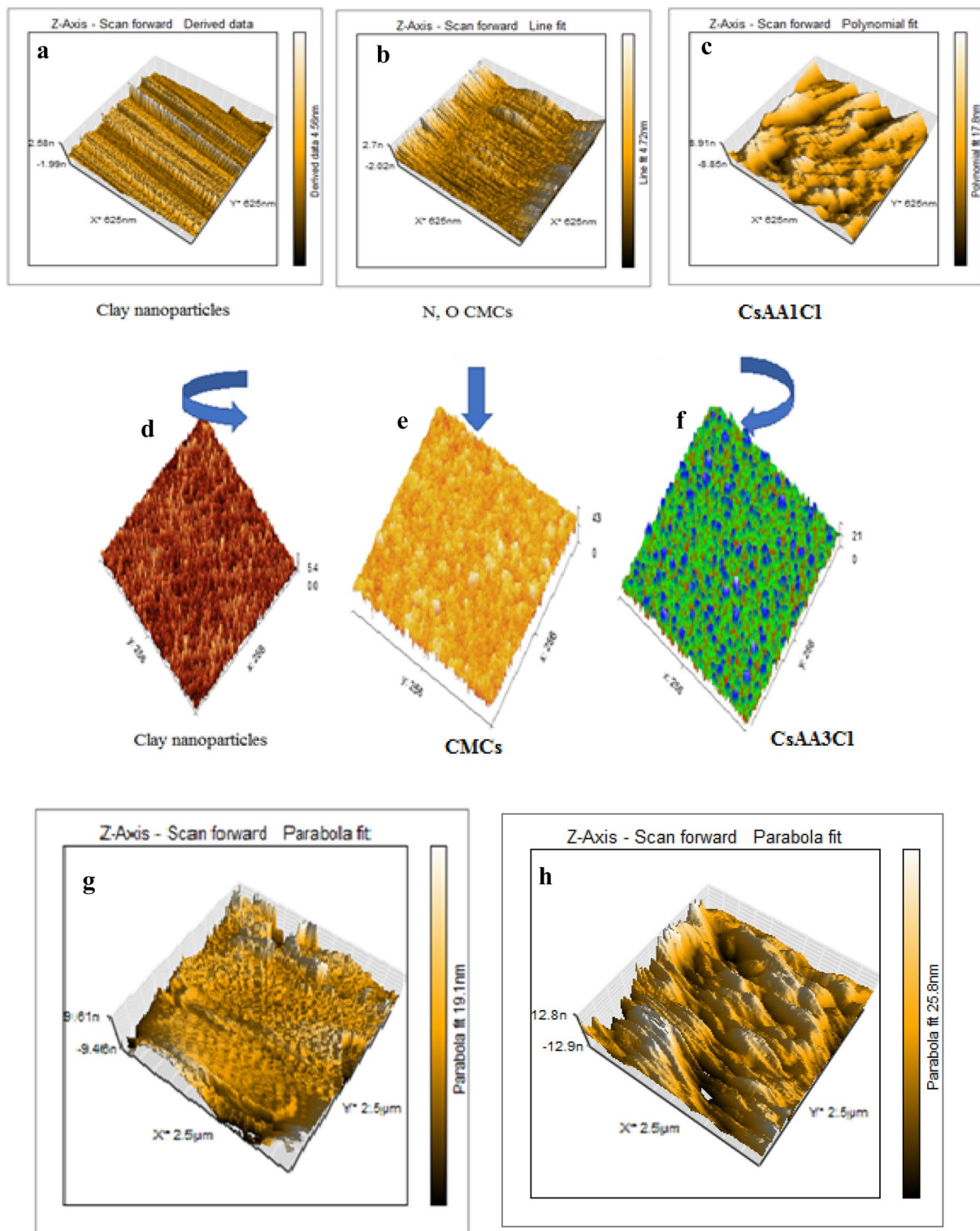


Fig. 1 AFM images of **a** clay nanoparticles, **b** N, O CMCs, **c** CsAA₁Cl, **d** clay nanoparticles (Gwyddion), **e** N, O CMCs (Gwyddion), **f** CsAA₁Cl (Gwyddion), **g** CsAA₂Cl, **h** CsAA₃Cl

Table 3 BET Data for the investigated sorbents

Sorbent	Total Surface area (m ² /g)	Average pore volume (cc/g)	Average pore diameter (nm)
N, O CMCs	22.4	0.015	4.22
CsAA ₁ Cl	31.6	0.024	4.43
CsAA ₂ Cl	68.9	0.073	5.06
CsAA ₃ Cl	77.4	0.088	6.71

appear in the spectra of CMCs and CsAA₃Cl. Moreover, the peak assigned for C=O group appears at 1750 cm⁻¹. This peak is shifted upfield in the spectrum of CsAA₃Cl due to the formation of crosslinking points with acrylic acid. Our data runs parallel to other workers finding [67, 68].

3.6 XRD Characterization

The XRD analysis is conducted to study the crystallographic structure of the composite. The XRD patterns of clay, N, O CMCs and CsAA₃Cl is displayed in Fig. 4a. It is obvious that clay exhibited a very crystalline structure while N, O CMCs is semi- to non- crystalline structure. However, the crystallinity of CsAA₃Cl lie between the two other components which confirm the full dispersion of the nanoclay particles within the polymer matrix. The peak at the range 32–42° which is characteristic to the kaolinite [45, 69] disappeared completely from the patterns of the two other systems. Amir et al. [70] observed other peaks at 20.88, 26.75, 34.26, 50.35, 54.32°, which approve the crystalline structure of montmorillonite clay MC. In another study, Noori et al. [71] detected peaks at angles 2θ = 22.38°, 26.63°, 28.11°, and 29.95° for natural clinoptilolite.

Additionally, an expansion and shifting of another peak at 20°, assigned for clay, was also detected. It is supposed this

was attributed to the presence of chitosan, which interrupted the overall crystallinity of the clay. Our findings fit the data obtained by other investigators for the crystallinity measurements of some relevant chitosan modified products [72, 73]. Moreover, some of the characteristic peaks of clay are hidden which reveals that Kaolin clay is intercalated and exfoliated [74, 75]. This observation assists the AFM finding.

3.7 Thermal Properties of the Investigated Products

The thermal properties of the polymer/clay nanocomposites can be judged by studying their thermal behavior. The TGA and DTG of N, O CMCs, CsAA₃ and CsAA₃Cl are given in Fig. 4b and c respectively. The TGA thermogram of N, O CMCs implied lower thermal stability and very rapid degradation in one instant step. However, the degradation pattern of CsAA₃ displayed three degradation stages; the first one appears in the range of 100–300 °C which may be attributed to evaporation of water of crystallization and the other two

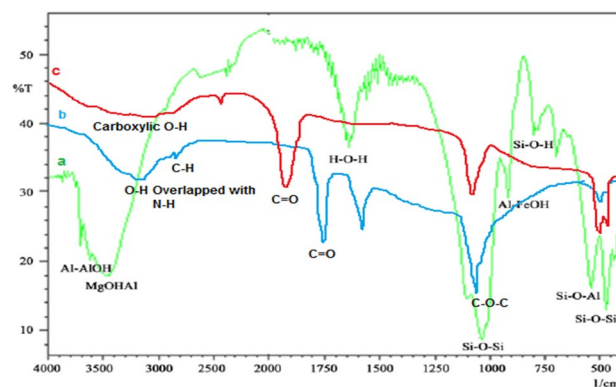
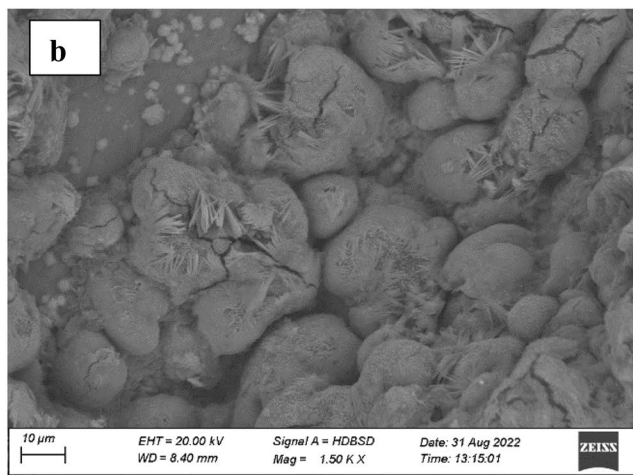
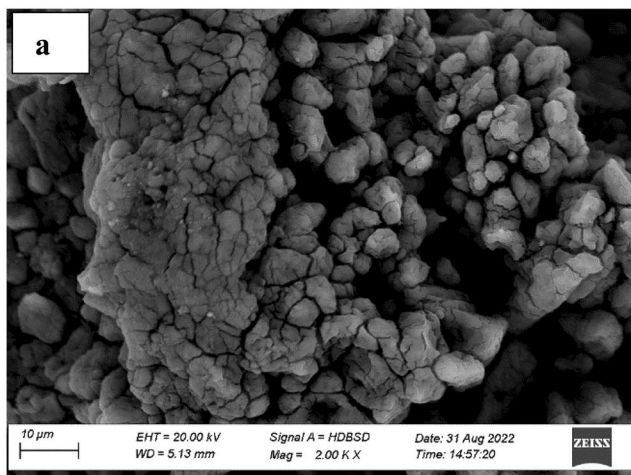
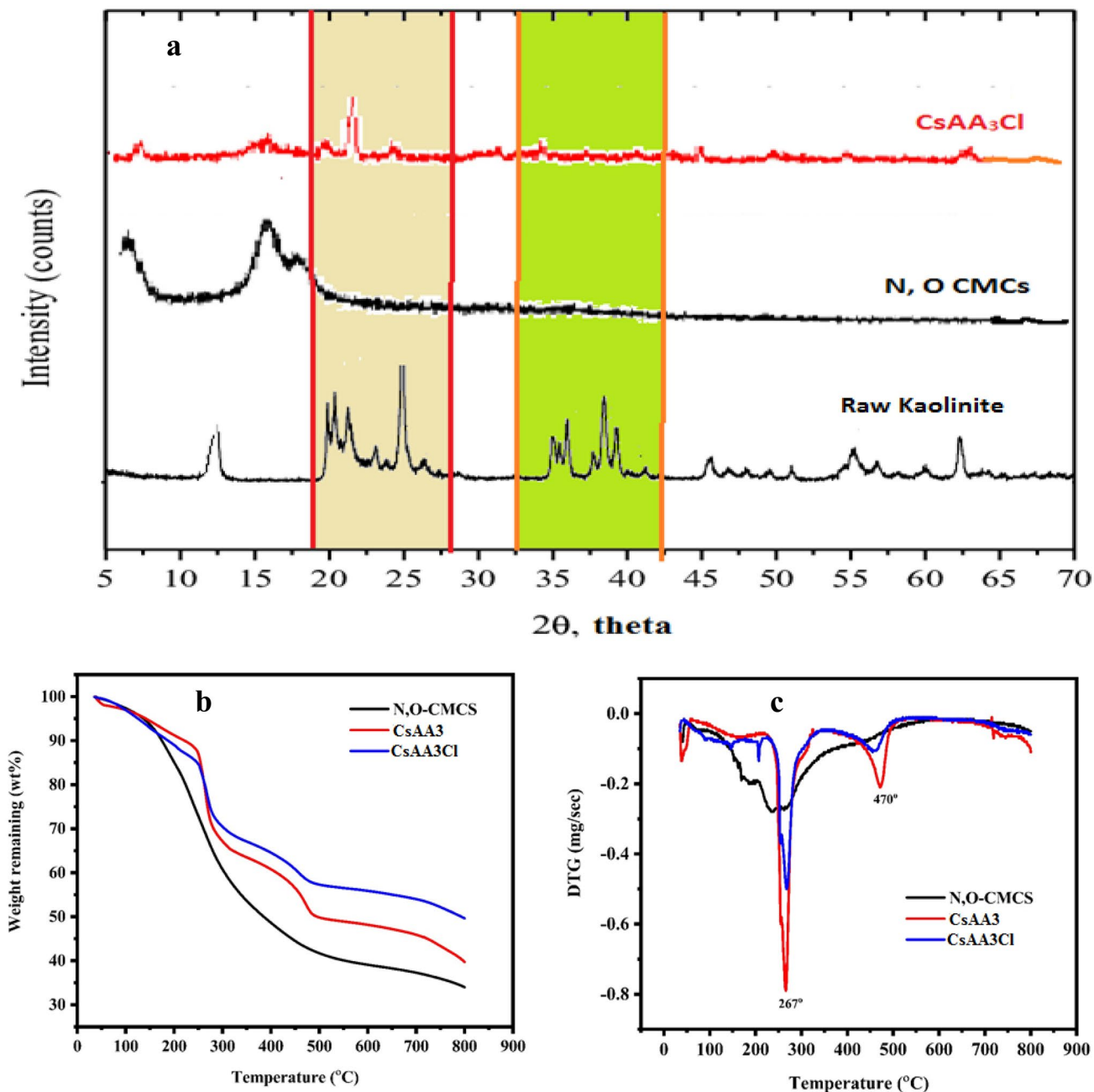
**Fig. 3** IR spectra of a Clay, b N, O CMCs and c CsAA₃Cl**Fig. 2** The FE-SEM image of a- CsAA₃ and CsAA₃Cl

Table 4 Weight loss and thermal decomposition temperature (T_d) for chitosan modified products

Sample	Weight loss %			Total	T_d (°C)
	<200 °C	200–600 °C	>600 °C		
N,O CMCs	10	60	5	75	255
CsAA ₃	7	50	10	67	267, 470
CsAA ₃ Cl	3	40	8	51	280, 500

stages are ascribed to degradation of hydrogel matrix [76]. On the other hand, the thermal stability of the composite is enhanced with the addition of clay particles due to its high crystallinity [77]. Some investigators attributed the improved thermal stability of the composite due to the strong electrostatic attraction between the anionic groups of modified chitosan and the cationic metals in the clay molecule [78]. The weight loss and thermal decomposition of the investigated samples are given in Table 4.

**Fig. 4** aThe XRD patterns of clay, N, O CMCs and CsAA₃Cl, b TGA of N, O CMCs, CsAA₃ and CsAA₃Cl, c DTG of N, O CMCs, CsAA₃ and CsAA₃Cl

3.8 Removal Experiments

3.8.1 Selection of the Optimum pH

The pH of the medium plays a predominant role on metal uptake process because it directly impacts the protonation of the functional groups and controls the degree of ionization of the sorbent materials [79, 80]. The effect of pH was verified by the batch model in a range varied from 1.0 to 9.0 for Pb (II) cations and from 4.0 to 11.0 for Cr (VI) cations using fixed conditions of 50 mg adsorbent, 2 h contact time, and 50 ml aqueous solution evaluating 100 mg/L Cr (VI) or Pb (II) cations at ambient temperature. The pH range for conducting the experiments was carefully selected according to the degree of solubility of each cation as per previous works [77, 78]. The maximum metal uptake performance was attained at pH 8.0 for Pb (II) and pH 9.0 for Cr (VI), according to the data displayed in Fig. 5a and b respectively. This finding is opposite to the data mentioned by some investigators who claimed acidic pH for maximum removal of Cr(VI). Nevertheless, it is proposed that higher adsorption capacity in alkaline medium may be attributed to the hydrogen bonding formation between chromate anions and the hydrogen protons of the functional groups of modified chitosan and also the attraction between the negatively charges chromate

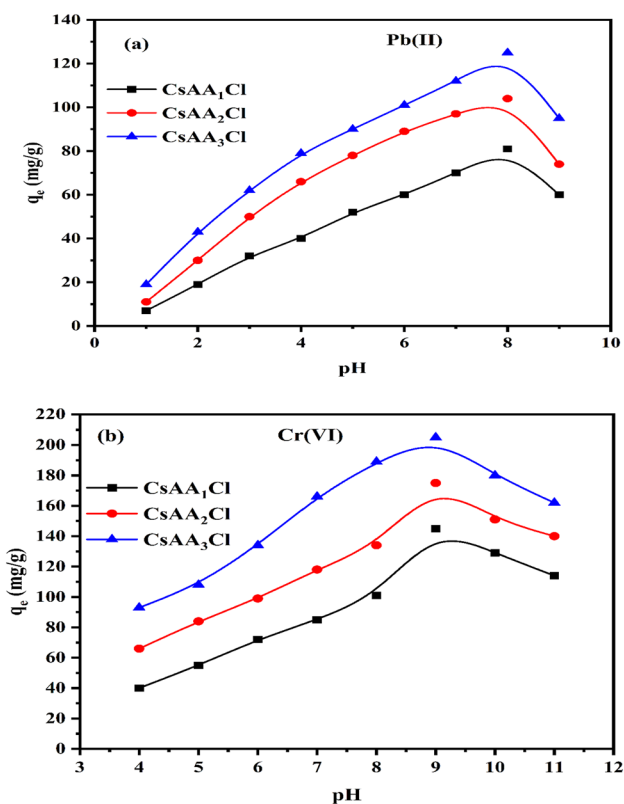


Fig. 5 Effect of pH value on maximum metal by CsAA₃Cl

anions and the metal cations in the nanoclay particles [43, 76, 79, 81]. The data reveal that the highest metal removal capacity was achieved by CsAA₃Cl for both Pb (II) and Cr (VI) it was found to be 125 mg/g and 205 mg/g respectively. This finding assists the AFM outcomes regarding the optimization of the sorbents in accordance to the CMCs/AA ratio. Therefore, CsAA₃Cl will be selected to verify the influence of other application factors on the removal process.

3.8.2 Effect of Contact time

The kinetics of adsorption process of Cr (VI) and Pb (II) onto CsAA₃Cl can be verified by monitoring the metal removal performance as a function of time. At room temperature, a 50 ml aqueous solution of 100 mg/L initial concentration of each metal ions at pH 9.0 for Cr (VI) ions and 8.0 for Pb (II) cations was stirred separately with 50 mg adsorbent for 120 min. The data are presented in Fig. 6a. It can be depicted that the complete equilibrium metal uptake for both metal ions were attained within 90 min although about 80% of total adsorption was achieved in the first 50 min due to the abundance of the active sites available for adsorption and the higher initial concentration gradient. This data is comparable to those obtained in our previous work [23].

3.8.3 Effect of Sorbent Dose

It is well established that the amount of sorbent material highly affects the quantity of metal removed by the sorbent [32]. Under any application conditions, it is essential to apply the minimum amount of sorbent to achieve the maximum metal uptake. In this regard, CsAA₃Cl was applied with masses ranged from 10 to 50 mg to remove Cr (VI) and Pb (II) cations from 50 mL of a solution containing 100 mg/L of each metal ions at pH 9.0 and 8.0 for Cr (VI) and Pb (II) cations, respectively at ambient temperature. The data are displayed in Fig. 6b. It can be observed that increasing the amount of adsorbent improved the metal uptake capacities of both metal ions. This may be explained on the basis of the active sites available for metal capturing [80]. It is believed that the incorporation of clay nanoparticles into the polymer matrix enhanced the sorption performance of the hydrogel due to the recognized high surface area/volume ratio of clay material [82, 83].

3.8.4 Effect of Initial Metal Ion Concentration at Different Temperatures

The initial metal ion concentration is a very important factor for overwhelming the restrictions encountered during the mass transfer between different phases. Therefore, a higher preliminary concentration of Cr (VI) and Pb (II) cations is said to enhance the adsorption process. The adsorption of

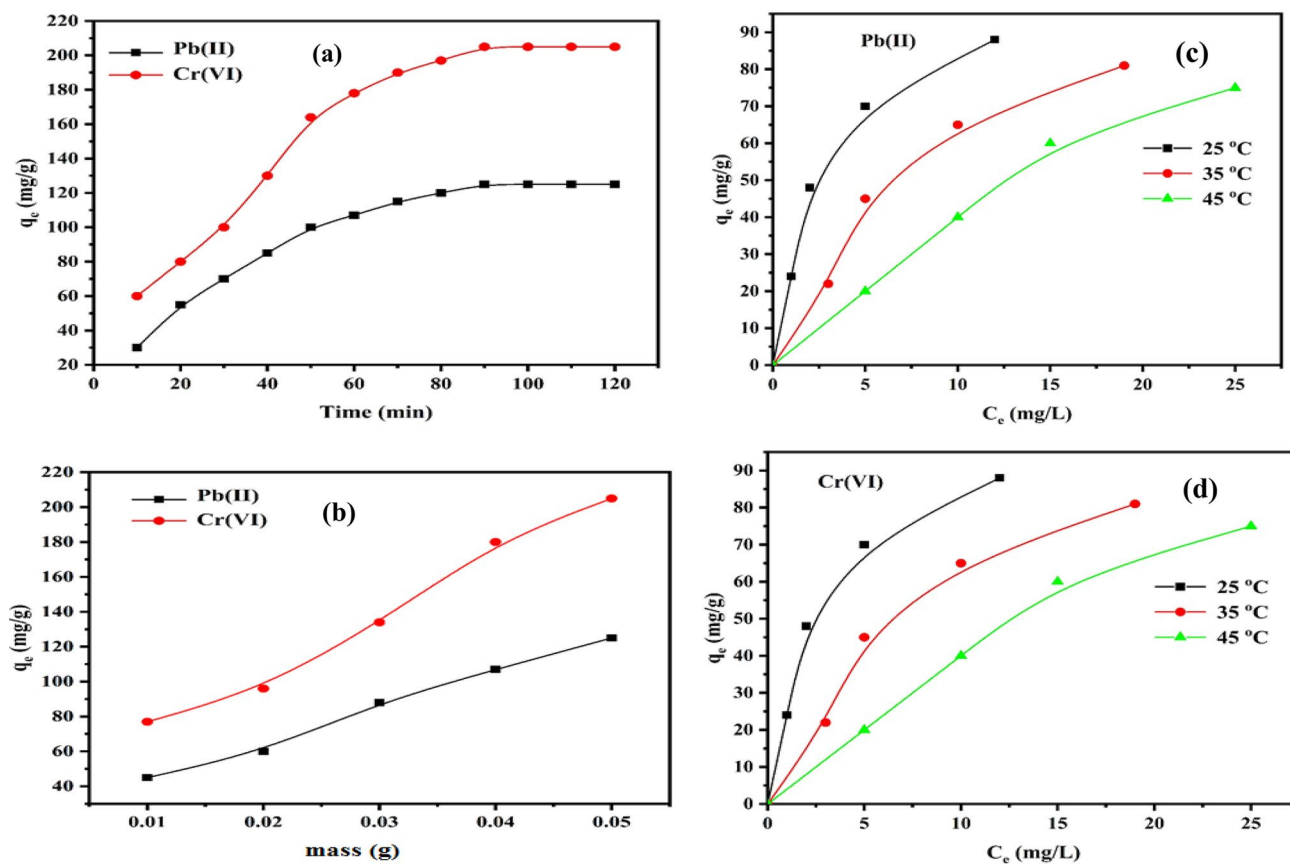


Fig. 6 Factors affecting metal uptake process by CsAA₃Cl **a** Time, **b** Mass of adsorbent, **c** Pb(II) concentrations at different temperatures and **d** Cr(VI) concentrations at different temperatures

both metal ions was investigated under static conditions as a function of metal ions concentration varied from 25 to 100 mg/L. The experiments were conducted at the following experimental conditions: 50 mg adsorbent, 50 ml aqueous solution, 90 min contact time and at pH 9.0 for Cr (VI) and 8.0 for Pb (II) cations, respectively, in a temperature range (25–45 °C). The data are presented in Fig. 6c and d for Cr (VI) and Pb (II) cations respectively. It is observed that the amount of metal ions adsorbed onto CsAA₃Cl increases remarkably as the concentration of the pollutant increased while an opposite behavior was noticed with temperature changes. The reverse effect of temperature on the metal uptake capacity is attributed to several factors such as the stability of chelate structure, mobility of metal cations, and dilation or shrinking of pores [84–86].

3.9 Adsorption Kinetics

Kinetic models are very important to verify the kinetic properties of the adsorption process and rate-controlling terms. Although several equations were used to describe the solid–liquid extraction system, pseudo-first-order (PFO)

and pseudo-second order (PSO) are the most commonly used models to define the kinetics of adsorption of Cr (VI) and Pb(II) cations onto CsAA₃Cl. The pseudo-first-order, pseudo-second-order parameters, Elovich and intraparticle diffusion models are computed from the following equations:

$$q_t = q_e(1 - \exp^{-K_1 t}) \quad (4)$$

$$q_t = \frac{K_2 q_e^2 t}{1 + K_2 q_e t} \quad (5)$$

$$q_t = \frac{\ln \alpha \beta}{\beta} + \frac{1}{\beta} \ln t \quad (6)$$

$$q_t = k_{di} t^{0.5} + C_i \quad (7)$$

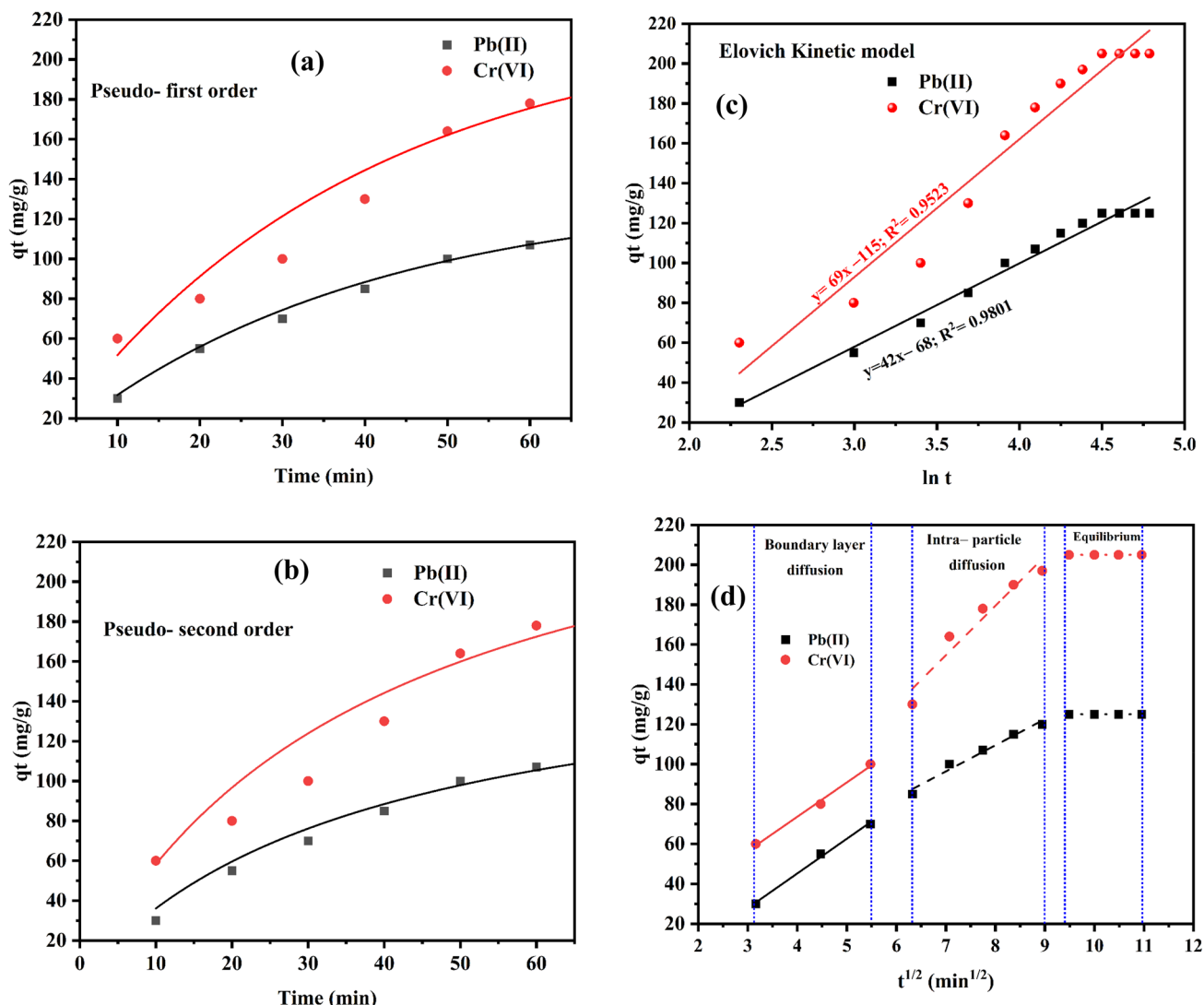
where t is the time (min), q_e , q_t , and q_e^2 are the amounts of metal adsorbed onto adsorbent at equilibrium, at time t , and the maximum adsorption capacity (mg/g) respectively. Also, K_1 , K_2 and k_{di} are the adsorption rate constant of pseudo-first-order (g/mg/min), pseudo-second-order (g/mg/min) and

Table 5 Kinetic parameters for adsorption of Cr(VI) and Pb(II) cations onto CsAA₃Cl

Kinetic model	Kinetic parameters	Pb(II)	Cr(VI)
Pseudo-first order PFO	K_1 (min ⁻¹)	0.027	0.027
	q_e (Cal.), (mg/g)	133	219
	q_e (exp), (mg/g)	125	205
	R^2	0.998	0.996
Pseudo-second order PSO	K_2 (g mg ⁻¹ min ⁻¹)	2×10^{-5}	9×10^{-5}
	q_e (Cal.), (mg/g)	171	283
	q_e (exp), (mg/g)	125	205
	R^2	0.992	0.993
Elovich kinetic	α (mg (g ⁻¹ min ⁻¹))	8.3	13.11
	β (g mg ⁻¹)	0.024	0.0144
	R^2	0.9801	0.9523
Intraparticle diffusion	k_{di} mg (g ⁻¹ min ^{-0.5})	13.1	24.8
	C_i	4.6	-18.9
	R^2	0.9676	0.9146

the intraparticle diffusion rate constant, mg (g⁻¹ min^{-0.5}) respectively. The parameter α is the initial adsorption rate, mg (g⁻¹ min⁻¹), and β is related to extent of surface coverage and activation energy for chemisorption, g mg⁻¹. The data are given in Table 5. When adsorption process follows pseudo first order, it implies that the metal ions are physically adsorbed onto the sorbent. On the other hand, the pseudo second order indicates that the adsorption process is a chemical progression [87, 88]. The pseudo first, second order kinetic, Elovich and intraparticle diffusion models for Cr(VI) and Pb(II) are illustrated in Fig. 7a–d respectively.

The data in Table 5 reveals that the values of correlation coefficient, R^2 related to pseudo-first-order model are greater than those attained from the pseudo-second-order and Elovich models for both Cr(VI) and Pb(II). This indicates that the adsorption was better fit by pseudo-first order

**Fig. 7** Pseudo first (a); second order kinetic (b); Elovich kinetic (c) and Intraparticle diffusion (d) models for adsorption of Cr(VI) and Pb(II) cations by CsAA₃Cl from simulated solution

and implies that the adsorption process is probably due to formation of chelate structure or electrostatic attraction between the active groups on the chitosan derivative and the metal ions. This finding is in a good agreement with our previous work [23, 89, 90].

The intraparticle diffusion model for the adsorption of both Pb(II) and Cr(VI) by CsAA₃Cl revealed three regions: 1st step hydrogel diffusion, which corresponds to the rapid adsorption of metal ions from the aqueous phase to the boundary layer of the hydrogel; 2nd step gradual adsorptions, which correspond to the diffusion of metal ions within the porous sites of the hydrogel; and 3rd step equilibrium stage, which is the adsorption of metal ions into the interior surface of the hydrogel.

3.10 Adsorption Isotherm Models

The adsorption isotherm models are very important in providing complete information on the interaction between metal ion solution and the adsorbent. Therefore, several isotherm models were proposed to denote the mechanism of the process. In the present work, two-parameter (Freundlich and Langmuir) and three-parameter (Redlich–Peterson) adsorption isotherm models were applied as they are the most common models tested by several authors [89–91]. All models were fit utilizing the non-linear fitting method by Origin Pro. 2022 software. These models are represented in Figs. 8a–c and 9a–c for Pb(II) and Cr(VI) respectively. Furthermore, the data for all the investigated models are given in Table 6.

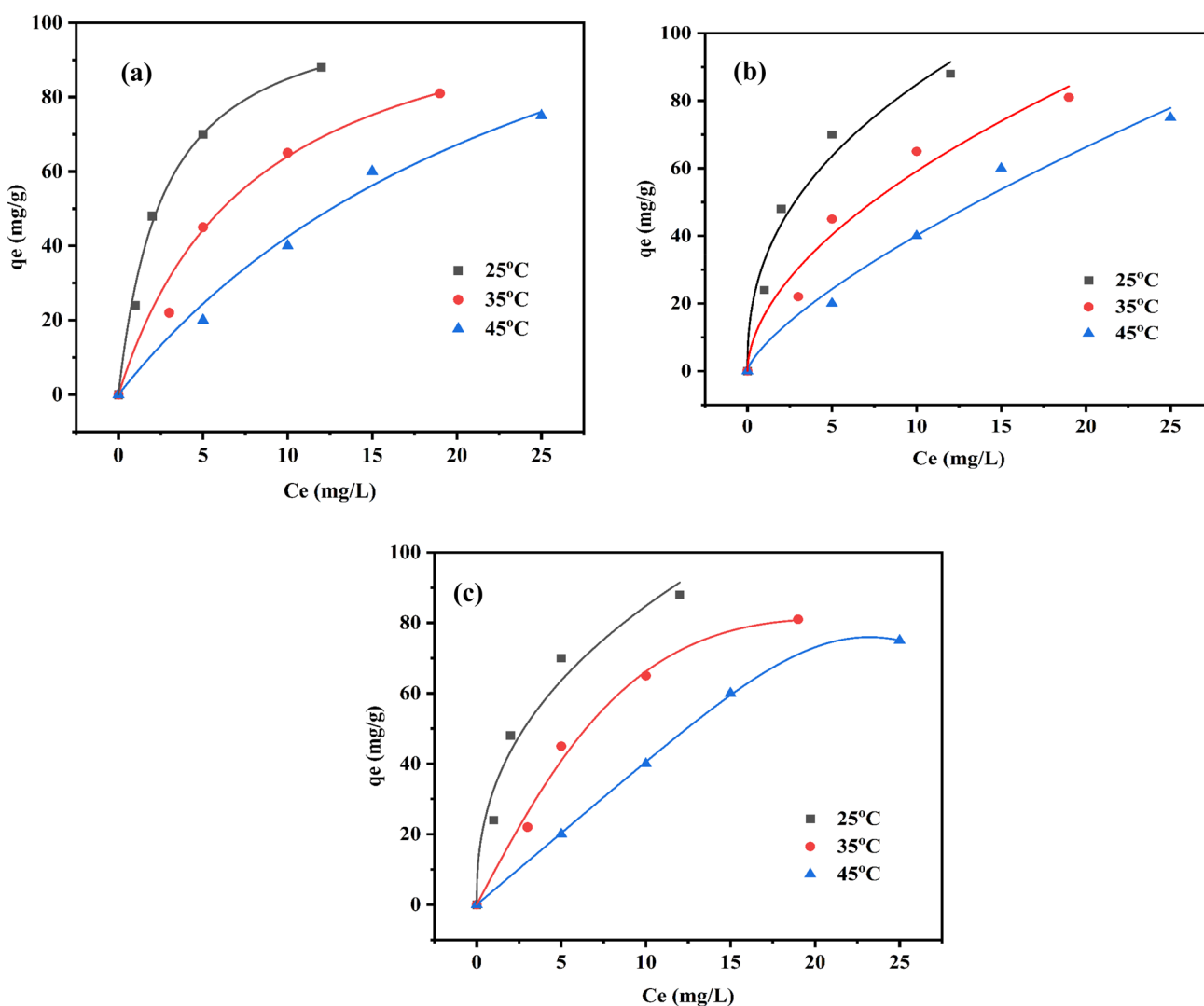


Fig. 8 Adsorption isotherm models of Pb(II) cations onto CSAA₃Cl at temperature 25 °C, 35 °C & 45 °C; Langmuir (a), Freundlich (b) and Redlich–Peterson (c)

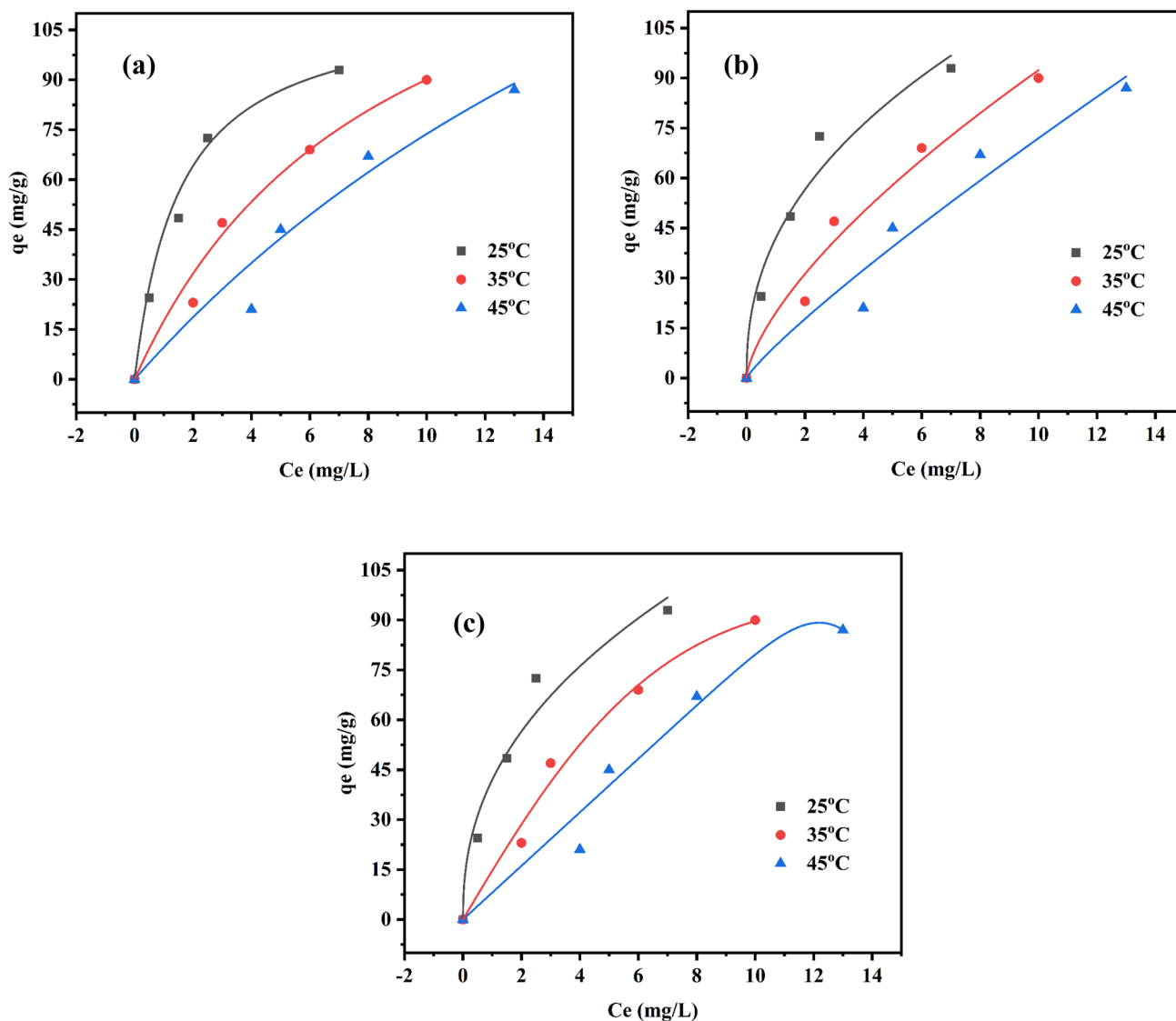


Fig. 9 Adsorption isotherm models of Cr(VI) cations onto CSAA₃Cl at temperature 25 °C, 35 °C & 45 °C; Langmuir (a), Freundlich (b) and Redlich–Peterson (c)

3.10.1 Langmuir Model

As per Langmuir isotherm model, adsorption is a chemical process in a monolayer assortment. The adsorption data were fitted according to Eq. 8.

$$q_e = \frac{K_L Q_m C_e}{1 + K_L C_e} \quad (8)$$

where; C_e is the concentration of the metal cations at equilibrium (mmol/L), q_e is the amount of metal ions adsorbed onto the sorbent at equilibrium (mmol/g), Q_m is the maximum adsorption capacity of the investigated metal ions (mmol/g), and K_L is the Langmuir constant which is relevant to the energy of adsorption (L/mmol).

3.10.2 Freundlich Model

The adsorption on a heterogeneous surface was proposed by Freundlich adsorption model. The mathematical representation of this model was given in Eq. (9):

$$q_e = K_f C_e^{1/n} \quad (9)$$

The Freundlich constants (K_f and n) are dependent on the capacity and the intensity of the adsorption process, respectively.

3.10.3 Redlich–Peterson Model

Redlich–Peterson equation (Eq. 10) [92] is widely used as a cooperation between Langmuir and Freundlich systems. It can be applied to homogenous and heterogenous systems. This model has three parameters and incorporates the advantageous significance of both models. Redlich–Peterson model can be represented as follows:

$$q_e = \frac{AC_e}{1 + BC_e^\beta} \quad (10)$$

where A (L/g) and B (L/mg)^β are the Redlich–Peterson isotherm constants and β is the exponent indicating the inhomogeneity of the sorbent, which lies between 0 and 1.

The best-fitting isotherm model and the mechanism of adsorption process can be determined by comparing the adsorption data from Freundlich, Langmuir and Redlich–Peterson isotherms.

The sorption equilibrium data were best fitted to the Langmuir model where the highest values for (R²) were obtained for both Pb (II) and Cr(VI) at all temperatures studied. Also, there is a good agreement between the calculated and experimental values of q_e. The experimental values for Pb(II) and Cr (VI) adsorption were found 125 and 205 mg/g, respectively.

3.11 Adsorption Thermodynamics

The study of adsorption thermodynamics was conducted in order to have a comprehensive understanding of the internal energy and the structure change that occurs after adsorption. The spontaneity and influence of heat on adsorption are very important to recognize the favorability of the overall process. Under optimal conditions, the thermodynamics of Pb(II) and Cr(VI) ion adsorption were investigated at 298 K, 308 K, and 318 K. The thermodynamic parameters, such as enthalpy change (ΔH°), entropy change (ΔS°), and Gibb's free energy change (ΔG°) can be evaluated by the following equations:

$$\ln \frac{q_e}{C_e} = \frac{\Delta S^\circ}{R} - \frac{\Delta H^\circ}{RT} \quad (11)$$

$$\Delta G^\circ = \Delta H^\circ - T\Delta S^\circ \quad (12)$$

where T represents the absolute temperature (K) and R denotes the universal gas constant (8.314 J mol⁻¹ K⁻¹). The values of ΔH° and ΔS° can be derived from the slope and intercept of the linear graph depicting ln (q_e/C_e) vs. 1/T, as depicted in Fig. 10, and the estimated parameters are provided in Table 7. It can be seen that the adsorption of Pb(II) and Cr(VI) ions onto CsAA₃Cl are exothermic as negative value of the ΔH°, implying that a temperature increase is

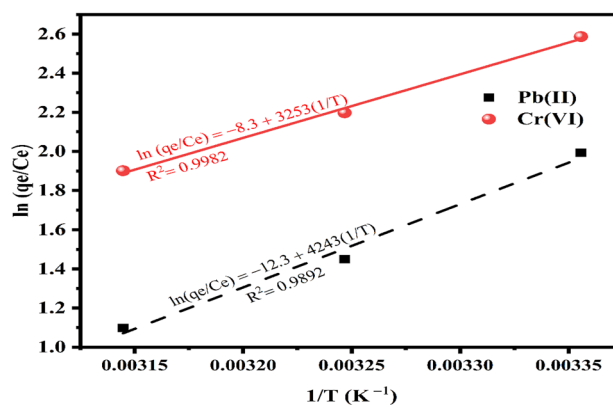


Fig. 10 Van't Hoff plots for the removal of Pb(II) and Cr(VI) by CsAA₃Cl

undesirable for the adsorption process. Gibbs free energy shows adsorption spontaneity, and a higher negative value indicates a more energetically beneficial sorption [93].

Negative ΔG° confirms thermodynamic feasibility and spontaneous adsorption. Positivity in ΔS° has been shown to increase the randomness of the solid-solution interface [94].

3.12 Monitoring the Removal Process According to the AFM Outcomes

According to our previous works [8, 23], the AFM was successfully utilized to confirm the metal uptake process by considering the following: the height and roughness measurements, phase analysis and change in topographic features. In this work, we applied the same methodology in order to confirm the adsorption process onto the surface and also within the polymer matrix itself by comparing the height of the dry sample and the height of the sample after metal uptake. Also, the layer of the metal adsorbed onto the surface can be imaged by the phase analysis. The images of the dry sample of CsAA₃Cl, the Cr(VI)-loaded CsAA₃Cl and the Pb(II)-loaded CsAA₃Cl their phase images are illustrated in Fig. 11. The AFM measurements are also given in Table 8. Examining the images of the topographic features of the dry and metal loaded samples, the metal cations loaded onto the surface can be seen as white batches. On the other hand, when inspecting the data of height and roughness, it is clear that the height values of the chromium loaded hydrogel is higher than that of the lead loaded sample which implies that the amount of chromium captured within the hydrogel voids are much greater than those of lead. This may be attributed to the stronger chelate structure formed by Cr(VI) than the weaker electrostatic attraction formed between the functional groups on the polymer and the Pb(II) cations [95, 96]. Regarding the roughness measurements, it can be seen that the value of R² (total area roughness)

Table 6 Parameters of adsorption isotherm models of Pb(II) and Cr(VI) cations

	Isotherm models	Parameter value	25 °C	35 °C	45 °C	
Pb(II) cations	Langmuir	Q_m (mg/g)	161	115	107	
		K_L (L/mg)	0.035	0.124	0.37	
		R^2	0.9999	0.9997	0.9999	
	Freundlich	K_F	7.6	16.6	32.7	
		n_F	1.4	1.8	2.4	
		R^2	0.976	0.956	0.976	
	Redlich-Peterson	A_{RP}	4.06	1.07	9.08	
		a_R	2.4	3.26	0.01	
		g	5.12	0.59	1.7	
		R^2	0.996	0.940	0.983	
	Cr(VI) cations	Langmuir	Q_m (mg/g)	283	133	166
			K_L (L/mg)	0.035	0.64	0.11
R^2			0.999	0.999	0.999	
Freundlich		$K_F [(mg\ g^{-1})(mg^{-1})^{1/n}]$	9.7	42.0	19.6	
		n_F	1.14	2.33	1.48	
		R^2	0.935	0.959	0.968	
Redlich-Peterson		A_{RP}	8.05	2.33	14.79	
		a_R	1.23	5.56	0.014	
		g	10.97	0.57	1.79	
		R^2	0.935	0.939	0.971	

Table 7 Thermodynamic parameters of Pb (II) and Cr (VI) removal onto CsAA₃Cl

Thermodynamic parameter	Temp.(K)	Pb (II)	Cr (VI)
$\Delta G^\circ \times 10^3$ (kJ.mol ⁻¹)	298	- 10.5	- 8.1
	308	- 10.8	- 8.3
	318	- 11.2	- 8.6
ΔH° (kJ mol ⁻¹)		- 0.1	35.3
ΔS° (kJ mol ⁻¹ K ⁻¹)	18.17	35.3	35.3

increases by increasing the amount of metal adsorbed onto the outer surface of the hydrogel.

3.13 Reusability Investigation

The reusability investigation is performed in order to judge the metal uptake capacity of the sorbent material at repeated cycles. It is dependent on many factors such as the chemical nature of the sorbent material and the nature of interaction between the adsorbate and the active sites of the sorbent [97]. The removal performance of CsAA₃Cl towards both Cr(VI) and Pb(II) at three cycles at their optimum working conditions is given in Fig. 12. It can be displayed that the metal uptake capacity is nearly the same at the first and the second application cycle. However, there is a noticeable

decline in the amount of metal adsorbed onto the active sites at the third cycle. This may be attributed to the nature of interaction between the metal and the sorbent which is mostly formation of chelate structure with Cr(VI) [98] and an electrostatic interaction with Pb(II) [99–101]. The removal performance of the prepared nanocomposite is very comparable to the values obtained by other green sorbents as seen in Table 9.

4 Conclusions

Three green chitosan-based hydrogel nanocomposite were prepared by gamma irradiation as sorbents for two potent toxic metals from aqueous solution, namely, lead and chromium cations. The prepared composites were characterized by different analyses to investigate the effect of the clay material on the crystalline structure and the thermal stability of the prepared hydrogels. In addition, the AFM was used to nominate the optimum sorbent according to the surface features and the height and roughness measurements. The experimental outcomes approved that CsAA₃Cl was the optimum sorbent that achieved maximum metal uptake at the optimized conditions; 125 mg/g and 205 mg/g for lead and chromium respectively at the optimum application conditions within 90 minutes at pH value 9 for chromium and

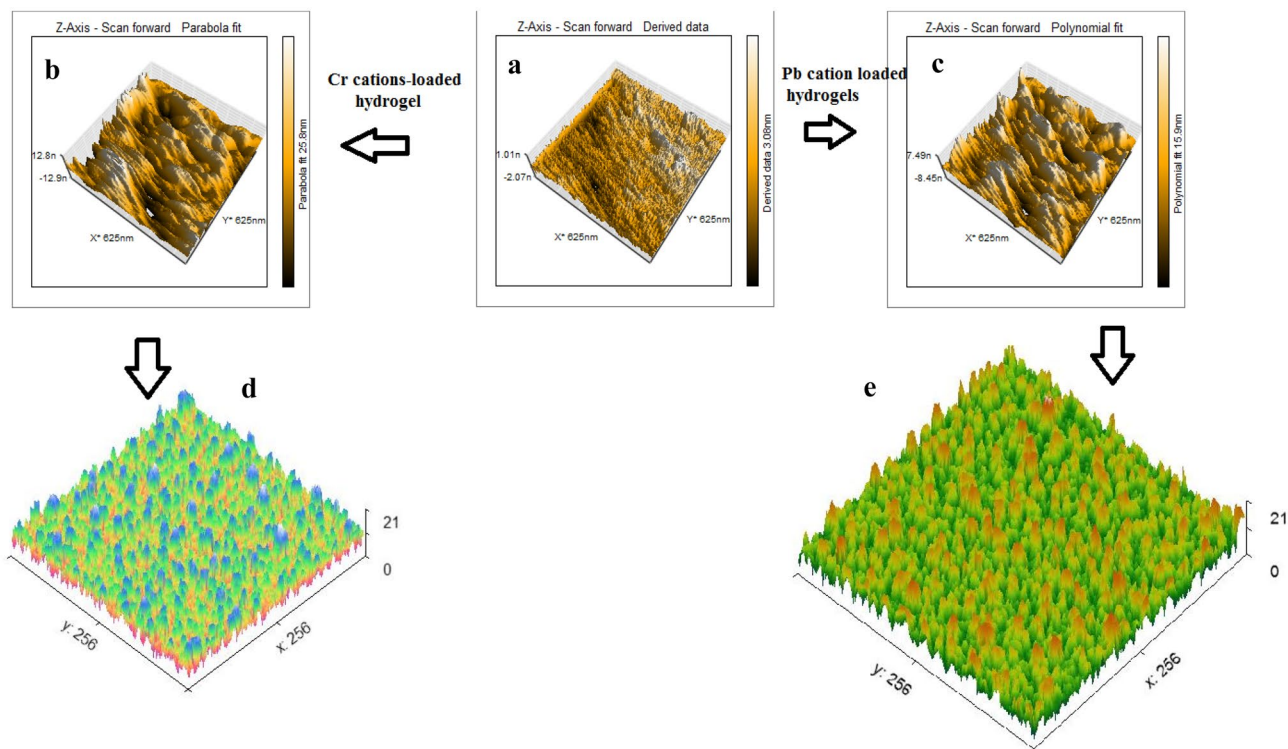


Fig. 11 **a** Topography of dry CsAA₃Cl, **b** Cr(VI)-loaded CsAA₃Cl, **c** Pb(II)-loaded CsAA₃Cl, **d** Phase differentiation of Cr(VI)-loaded CsAA₃Cl, **e** Phase differentiation of Pb(II)-loaded CsAA₃Cl

Table 8 The AFM outcomes of dry and metal loaded CsAA₃Cl

Sample	R ² (Area roughness (nm))	Height (nm)
CsAA ₃ Cl	14.22	3.08
Cr(VI)-loaded CsAA ₃ Cl	24.16	25.8
Pb(II)-loaded CsAA ₃ Cl	18.17	15.9

8 for lead. The data proved that the adsorption process followed the Langmuir monolayer model and the suggested mechanisms are merely formation of chelate structure and electrostatic attraction between the metal cation and the reactive groups on the sorbent molecule. The thermodynamic study reveals spontaneous adsorption and indicates favored process.

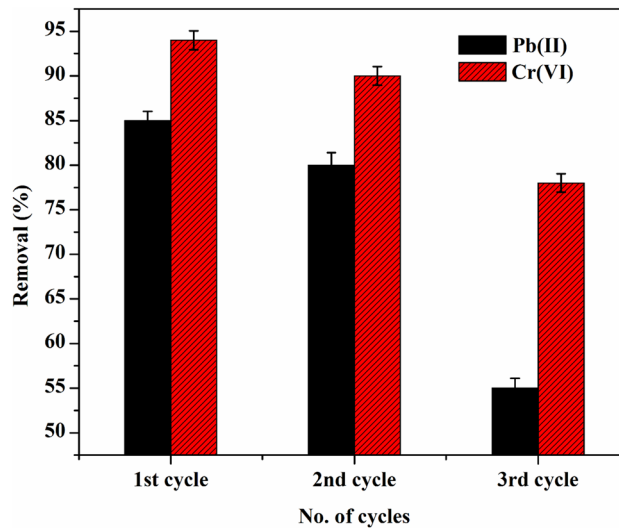


Fig. 12 Reusability of CsAA₃Cl towards lead and chromium cations at three application cycles

Table 9 Removal performance of some sorbents for Pb(II) and Cr (VI)

Adsorbent	Adsorption capacity (mg/g)	References
Cr (VI)		
NaOH treated pine (NTP) and magnetite-pine composite (NTP-NC)	Cr(VI) adsorption capacity of 6.48 and 13.88 mg/g pH 2 and adsorbent dose of 0.5 g for NTP and NTP-NC.	[102]
Live and pretreated biomass of <i>Aspergillus</i> flavours. [63]	Maximum adsorption capacity ($Q_{\max} = 0.335 \text{ mg g}^{-1}$) 50.90% of chromium was removed at the optimum conditions	[103] [63]
CsAA ₃ Cl	205 mg/g	[This work]
Pb (II)		
Graphene oxide	987.33 mg/g	[104]
Saw dust	3.19 mg/g	[105]
Activated carbon supported sulfide	295.30 mg/g	[106]
Carboxymethyl cellulose/acrylic acid/titanium dioxide nanocomposite hydrogel	Not available	[107]
CsAA ₃ Cl	125 mg/g	[This work]

Author Contributions MEI-SA-R: Supervision, Investigation, Validation, Methodology, Formal analysis, Writing—original draft, Writing—review & editing, DH: Analysis, Experimental and data curation. RK: Analysis, citation, data curation, review and figures. AS: Data curation, Methodology, Software, Formal analysis, writing original draft, Writing—review & editing.

Funding Open access funding provided by The Science, Technology & Innovation Funding Authority (STDF) in cooperation with The Egyptian Knowledge Bank (EKB). No funding was received for the present work.

Data Availability The data that support the findings of this study are available in the manuscript.

Declarations

Conflict of interest The authors declare that they have no known competing financial interests or personal relationships that could have appeared to influence the work reported in this paper.

Ethical Approval Ethical approval is not applicable for this article.

Consent to Participate The authors confirm that all information they provide for this study are realistic experimental data and findings.

Consent to Publish The authors give their consent for the publication of identifiable details, which can include photograph(s) and/or videos and/or case history and/or details within the text (“Material”) to be published in the above Journal and Article.

Open Access This article is licensed under a Creative Commons Attribution 4.0 International License, which permits use, sharing, adaptation, distribution and reproduction in any medium or format, as long as you give appropriate credit to the original author(s) and the source, provide a link to the Creative Commons licence, and indicate if changes were made. The images or other third party material in this article are included in the article's Creative Commons licence, unless indicated otherwise in a credit line to the material. If material is not included in the article's Creative Commons licence and your intended use is not permitted by statutory regulation or exceeds the permitted use, you will

need to obtain permission directly from the copyright holder. To view a copy of this licence, visit <http://creativecommons.org/licenses/by/4.0/>.

References

1. A. Chiori, Urban water planning in Lagos, Nigeria: an analysis of current infrastructure developments and future water management solutions (2018)
2. J.O. Nriagu, *Nature* **338**, 47 (1989)
3. B.R. Stern, *J. Toxicol. Environ. Health A* **73**, 114 (2010)
4. D. Bogdanov, M. Ram, A. Aghahosseini, A. Gulagi, A.S. Oyewo, M. Child, U. Caldera, K. Sadovskaia, J. Farfan, L. De Souza Noel Simas Barbosa, M. Fasihi, S. Khalili, T. Traber, C. Breyer, *Energy* **227**, 120467 (2021)
5. M.E. Abdel-Raouf, S.M. El-Saeed, E.G. Zaki, A.M. Al-Sabagh, *Egypt. J. Pet.* **27**, 1345 (2018)
6. M. Keshawy, R. Samir, M.E.-S. Abdel-Raouf, *Egypt. J. Chem.* **65**, 325 (2022)
7. A. Sayed, M. Yasser, M.E. Abdel-raouf, R. Mohsen, *Chem. Pap.* **76**, 5119 (2022)
8. G.A.M. Asmaa, M.M. Sayed, Mohamed, J. Inorg. Organomet. Polym. Mater. **32**, 4589 (2022)
9. D. Qiao, H. Liu, L. Yu, X. Bao, G.P. Simon, E. Petinakis, L. Chen, *Carbohydr. Polym.* **147**, 146 (2016)
10. R. Awuah, E. Amankwaa-Kuffuor, “*Characterization of wastewater; its sources and its environmental effects*” I-learning seminar on urban wastewater management (2002)
11. S.M.H. Hendy, *Wastewater management and reuse in Egypt. Regional Workshop on Health Aspects of Wastewater Reuse in Agriculture Amman, Jordan* (2006)
12. I. Metcalf, Eddy, *Wastewater engineering: treatment and reuse*”, Fourth. (McGraw-Hill, New York, 2003)
13. P. Amoatey, R. Bani, in *Waste Water—Evaluation and Management* (Intech, 2011), pp. 379–397
14. J.S. Wilbur, S. Abadin, H. Fay, M. Yu, D. Tencza, B. Ingerman, L. Klotzbach, *J. Toxicological Profile for Chromium* (Agency for Toxic Substances and Disease Registry, 2012)
15. D. Beyersmann, A. Hartwig, *Arch. Toxicol.* **82**, 493 (2008)
16. C.J. Tchounwou, Toxicologic pathology, in *Handbook of pre-clinical development*. ed. by S.C. Gad (Wiley, New York, NY, 2008)

17. J. Guertin, J. Jacobs, C.P. Avakian, *Chromium(VI) Handbook* (2016)
18. S.J.S. Flora, G. Flora, G. Saxena, in *Chapter 4 - Environmental Occurrence, Health Effects and Management of Lead Poisoning*, ed. J.S. Casas and J.B.T.-L. Sordo (Elsevier Science B.V., Amsterdam, 2006), pp. 158–228. <https://doi.org/10.1016/B978-044452945-9/50004-X>
19. C. Yedjou, J. Milner, C. Howard, P. Tchounwou, *Int. J. Environ. Res. Public. Health* **7**, 2008 (2010)
20. C. Sanfeliu, J. Sebastià, R. Cristòfol, E. Rodríguez-Farré, *Neurotox. Res.* **5**, 283 (2003)
21. R.K. Farag, S.M. EL-Saeed, M.E. Abdel-Raouf, *Desalin. Water Treat* **57**, 16150 (2016)
22. O. Kurt, H. Celebi, *Polym. Sci. Ser. A* **63**, 556 (2021)
23. A. Sayed, F. Hany, M.E.-S. Abdel-Raouf, G.A. Mahmoud, *J. Polym. Res.* **29**, 372 (2022)
24. S.S. Ray, A.O.C. Iroegbu, *ACS Omega* **6**, 4511 (2021)
25. S. Sahu, U.K. Sahu, R.K. Patel, *New J. Chem.* **42**, 5556 (2018)
26. Y. Chen, B. Pan, H. Li, W. Zhang, L. Lv, J. Wu, *Environ. Sci. Technol.* **44**, 3508 (2010)
27. R. Bade, S.H. Lee, *J. Water Sustain.* **1**, 85 (2011)
28. K. Mehta, *Int. Res. J. Eng. Technol.* **2**, 983 (2015)
29. M.E. Abdel-Raouf, N.E. Maysour, R.K. Farag, A.-R.M.A.-Raheim, *Int. J. Environ. Agric. Sci., an Open Access Journal* **3**, 18 (2019)
30. S. Sahu, N. Bishoyi, M.K. Sahu, R.K. Patel, *Chemosphere* **278**, 130507 (2021)
31. B. Ekka, G. Dhar, S. Sahu, M. Mishra, P. Dash, R.K. Patel, *Ceram. Int.* **47**, 19079 (2021)
32. A. Hasan, S. Elsaheed, R. Kamal, M.E.-S. Abdel-Raouf, *Adv. Mater. Lett.* **7**, 402 (2016)
33. A.F. El-Kafrawy, S.M. El-Saeed, R.K. Farag, H.A.-A. El-Saeed, M.E.-S. Abdel-Raouf, *Egypt. J. Pet.* **26**, 23 (2017)
34. S. Sahu, P. Kar, N. Bishoyi, L. Mallik, R.K. Patel, *J. Chem. Eng. Data* **64**, 4357 (2019)
35. S. Sahu, N. Bishoyi, R.K. Patel, *J. Ind. Eng. Chem.* **99**, 55 (2021)
36. Y. Abshirini, H. Esmaeili, R. Foroutan, *Mater. Res. Express* **6**, 125513 (2019)
37. A. MS, A. Hasan, *J. Pollut. Eff. Control* **05** (2017). <https://doi.org/10.4172/2375-4397.1000180>
38. R. Mallampati, L. Xuanjun, A. Adin, S. Valiyaveetil, *ACS Sustain. Chem. Eng.* **3**, 1117 (2015). <https://doi.org/10.1021/acsschemeng.5b00207>
39. M.E. Abdel-Raouf, in edited by A. Ahmad, R. Kumar, and M. B. T.-E. T. for T. of T. M. from W. Jawaid (Elsevier, 2023), pp. 83–101
40. R. Foroutan, S.J. Peighambardoust, R. Mohammadi, S.H. Peighambardoust, B. Ramavandi, *Chemosphere* **296**, 133978 (2022)
41. R. Foroutan, S.J. Peighambardoust, R. Mohammadi, S.H. Peighambardoust, B. Ramavandi, *Environ. Res.* **211**, 113020 (2022)
42. B. Naeimi, R. Foroutan, B. Ahmadi, F. Sadeghzadeh, B. Ramavandi, *Mater. Res. Express* **5**, 045501 (2018). <https://doi.org/10.1088/2053-1591/aab81b>
43. R. Foroutan, R. Mohammadi, B. Ramavandi, M. Bastanian, *Korean J. Chem. Eng.* **35**, 2207 (2018)
44. Z. Esvandi, R. Foroutan, M. Mirjalili, G.A. Sorial, B. Ramavandi, *J. Polym. Environ.* **27**, 263 (2019)
45. R. Foroutan, S.J. Peighambardoust, S. Hemmati, H. Khatooni, B. Ramavandi, *Int. J. Biol. Macromol.* **189**, 432 (2021)
46. G. Crini, *Prog. Polym. Sci.* **30**, 38 (2005)
47. B. Doshi, A. Ayati, B. Tanhaei, E. Repo, M. Sillanpää, *Carbohydr. Polym.* **197**, 586 (2018)
48. J. Dai, H. Yan, H. Yang, R. Cheng, *Chem. Eng. J.* **165**, 240 (2010)
49. S.S.D. Elanchezhiyan, P. Karthikeyan, K. Rathinam, M. Hasmath, Farzana, C.M. Park, *Carbohydr. Polym.* **261**, 117892 (2021)
50. M.E. González-López, C.M. Laureano-Anzaldo, A.A. Pérez-Fonseca, C. Gómez, J.R. Robledo-Ortíz, *J. Environ. Chem. Eng.* **9**, 105029 (2021)
51. M. Jamali, A. Akbari, *J. Environ. Chem. Eng.* **9**, 105175 (2021)
52. A.H. Jawad, A.S. Abdulhameed, S.N. Surip, S. Sabar, *Int. J. Environ. Anal. Chem.* **1** (2020)
53. T. Kekes, C. Tzia, *J. Environ. Manag.* **262**, 110372 (2020)
54. C. Lei, Q. Xiao, S. Zhou, W. Zu, J. Li, J. Zeng, L. Yan, Y. Huang, B. Wang, *J. Appl. Polym. Sci.* **139**, 52347 (2022)
55. S. Chatterjee, M.W. Lee, S.H. Woo, *Bioresour. Technol.* **101**, 1800 (2010)
56. S. Chatterjee, D.S. Lee, M.W. Lee, S.H. Woo, *Bioresour. Technol.* **100**, 2803 (2009)
57. N. Nagasawa, T. Yagi, T. Kume, F. Yoshii, *Carbohydr. Polym.* **58**, 109 (2004)
58. L. Zhao, H. Mitomo, N. Nagasawa, F. Yoshii, T. Kume, *Carbohydr. Polym.* **51**, 169 (2003)
59. A. Hasan, M. El-Keshawy, M. Abdel-Raouf, *Mater. Chem. Phys.* **278**, 125521 (2021)
60. A. Abdelaziz, S. Elsaheed, E.G. ZAKI, M. Abo-Aly, M.E.-S. Abdel-Raouf, A. Al-Sabagh, *Egypt. J. Chem.* **64**, (2021)
61. M.-T.Z.I. Karume, W. Z., and N. R., *Acad. J. Chem.* **102** (2020)
62. K. Kalebaila, K. Maseka, M. Mbulo, *Open J. Appl. Sci.* **08**, 355 (2018)
63. S. Biswas, T. Rashid, T. Debnath, P. Haque, M. Rahman, *J. Compos. Sci.* **4**, 16 (2020)
64. S. Biswas, T. Rashid, A. Mallik, M. Islam, M.N. Khan, P. Haque, M. Khan, M. Rahman, *Int. J. Polym. Sci.* **2017**, 6472131 (2017). <https://doi.org/10.1155/2017/6472131>
65. D. Aldhayan, A. Aouissi, *Bull. Chem. React. Eng. Catal.* **12**, 119 (2017)
66. A. Awwad, N. Salem, M. Amer, M. Shammout, *Chem. Int.* **7**, 139 (2021)
67. A. Hamd, D. Rady, M. Shaban, K. Elyamany, H. Almohamadi, A. Elzanaty, S. Ahmed, R. El-Sayed, N.K. Soliman, *Biointerface Res. Appl. Chem.* **12**, 6393 (2021)
68. V. Teofilović, J. Pavličević, O. Bera, M. Jovičić, J. Budinski-Simendic, K. Mészáros, Szécsényi, A. Aroguz, *Hem. Ind.* **68**, 653 (2014)
69. M. Meigoli Boushehrian, H. Esmaeili, R. Foroutan, *J. Environ. Chem. Eng.* **8**, 103869 (2020)
70. A. Ahmadi, R. Foroutan, H. Esmaeili, S.J. Peighambardoust, S. Hemmati, B. Ramavandi, *Mater. Chem. Phys.* **284**, 126088 (2022)
71. M. Noori, M. Tahmasebpour, R. Foroutan, *Mater. Chem. Phys.* **278**, 125655 (2022)
72. Y.-S. Han, S.-H. Lee, K. Choi, I. Park, *J. Phys. Chem. Solids* **71**, 464 (2010)
73. A.M. Shehap, R.A. Nasr, M. Mahfouz, A.M. Ismail, *J. Environ. Chem. Eng.* **9**, 104700 (2020)
74. A. Tironi, M.A. Trezza, E.F. Irassar, A.N. Scian, *Procedia Mater. Sci.* **1**, 343 (2012)
75. E. Klosek-Wawrzyn, J. Malolepszy, P. Murzyn, *Procedia Eng.* **57**, 572 (2013)
76. U. Malayoglu, *Sep. Sci. Technol.* **53**, 1 (2018)
77. F. Shi, D. Jiang, J. Ji, J. Yan, H. Chen, *Int. J. Environ. Res. Public. Health* **19**, 4811 (2022)
78. K. H., *Int. J. Water Wastewater Treat.* **3** (2017). <https://doi.org/10.16966/2381-5299.139>

79. H. Arabyarmohammadi, A. Khodadadi-Darban, M. Abdollahy, R. Yong, B. Ayati, A. Zirakjou, S. van der Zee, *J. Polym. Environ.* **26**, 2107 (2018)
80. R. Ahmad, I. Hasan, *Sep. Sci. Technol.* **51**, (2015)
81. N.R. Villarante, A.P.R. Bautista, D.E.P. Sumalapao, *Orient. J. Chem.* **33**, 1111 (2017)
82. R. Ahmad, I. Hasan, A. Mittal, *Desalin. Water Treat.* **58**, 144 (2017)
83. N. Cankaya, R. Sahin, *Cellul. Chem. Technol.* **53**, 537 (2019)
84. H. Alalwan, M. Kadhom, A. Alminshid, *J. Water Supply Res. Technol.* **69** (2020). <https://doi.org/10.2166/aqua.2020.133>
85. W.C. Li, F. Law, Y. Chan, *Environ. Sci. Pollut. Res. Int.* **24** (2015). <https://doi.org/10.1007/s11356-015-5081-7>
86. X. Hu, R. Zhang, B. Xia, R. Ying, Z. Hu, X. Tao, H. Yu, F. Xiao, Q. Chu, H. Chen, J. Qian, *Sustainability* **14**, 9022 (2022)
87. D. Alves, B. Healy, L. Pinto, T.R.S. Cadaval, C. Breslin, *Molecules* **26**, 594 (2021)
88. A. Yousif, A. el Afandy, G. Wahab, A. Mubark, I. Ibrahim, *J. Radioanal. Nucl. Chem.* **303**, 1821 (2015)
89. A. Sayed, A. Mazrouaa, M. Mohamed, M. Abdel-Raouf, *Environmental Science and Pollution Research* **1** (2022)
90. A. Al-Gorair, A. Sayed, G. Mahmoud, *Polymer (Basel)* **14**, 567 (2022)
91. H. El-saied, E. El-Fawal, *Polym. Test.* **97**, 107134 (2021)
92. E.K. Guechi, O. Hamdaoui, *Arab. J. Chem.* **9**, S416 (2011). <https://doi.org/10.1016/j.arabjc.2011.05.011>
93. R. Foroutan, R. Mohammadi, S.J. Peighambaridoust, S. Jalali, B. Ramavandi, *Environ. Technol. Innov.* **19**, 101031 (2020)
94. R. Foroutan, S.J. Peighambaridoust, R. Mohammadi, M. Omidvar, G.A. Sorial, B. Ramavandi, *Int. J. Biol. Macromol.* **151**, 355 (2020)
95. L. Pietrelli, I. Francolini, A. Piozzi, M. Sighicelli, I. Silvestro, M. Vociante, *Appl. Sci.* **10**, 1925 (2020)
96. L. Pietrelli, N.M. Ippolito, A.P. Reverberi, M. Vociante, *Chem. Eng. Trans.* **76**, 1327 (2019)
97. S. Iftekhar, D.L. Ramasamy, V. Srivastava, M.B. Asif, M. Silanpää, *Chemosphere* **204** (2018). <https://doi.org/10.1016/j.chemosphere.2018.04.053>
98. V. Kuppasamy, R. Balasubramanian, *Chem. Eng. J.* **163**, 337 (2010)
99. R. Vieira, E. Meneghetti, P. Baroni, E. Guibal, V. González-delaCruz, A. Caballero, E. Rodríguez-Castellon, M. Beppu, *Mater. Chem. Phys.* **146**, 412 (2014)
100. Y. Tao, L. Ye, J. Pan, Y. Wang, B. Tang, *J. Hazard. Mater.* **161**, 718 (2008)
101. A. Sayed, G.A. Mahmoud, H. Said, A.A. Diab, *Mater. Chem. Phys.* **280**, 125731 (2022)
102. A. Pholosi, E. Naidoo, A. Ofomaja, *South African J. Chem. Eng.* **32** (2020). <https://doi.org/10.1016/j.sajce.2020.01.005>
103. K.K. Deepa, S.M., A.R. Binupriya, G.S. Murugesan, K. Swaminathan, S.-E. Yun, *Chemosphere* **62**, 833 (2006)
104. G. Fajardo, L. Giraldo, J. Moreno-Piraján, *Nanomaterials* **10**, 1022 (2020)
105. B. Yu, Y. Zhang, A. Shukla, S. Shukla, K. Dorris, *J. Hazard. Mater.* **84**, 83 (2001)
106. J. Qu, Y. Liu, L. Cheng, Z. Jiang, G. Zhang, F. Deng, L. Wang, W. Han, Y. Zhang, *J. Hazard. Mater.* **403**, 123607 (2020)
107. A. Hendy, E. Khozemy, G. Mahmoud, E. Saad, S. Sorror, *Egypt. J. Chem.* **62**, 1785 (2022)

Publisher's Note Springer Nature remains neutral with regard to jurisdictional claims in published maps and institutional affiliations.